Supporting information

Highly reversible zinc anode enabled by a trace-amount additive with pH buffering capability

Xiaohui Ma[a], Qiong Wang[a], Xi Zhang[a], Yu Lin[a], Fengyi Zhang[a], Jianhang Huang*[a], Yonggang Wang*[b]

[a] Key Laboratory of the Ministry of Education for Advanced Catalysis Materials, College of Chemistry and Materials Science, Zhejiang Normal University, Jinhua 321004, China

[b] Department of Chemistry and Shanghai Key Laboratory of Molecular Catalysis and Innovative Materials, iChEM (Collaborative Innovation Center of Chemistry for Energy Materials), Fudan University, Shanghai 200433, China

* Correspondence Authors: jhhuang@zjnu.edu.cn (J. H.), ygwang@fudan.edu.cnn (Y. W.)

Experimental section

Preparation of electrolyte and electrode. Bare electrolyte (2 M $ZnSO_4$) was prepared by dissolving zinc sulfate ($ZnSO_4 \cdot 7 H_2O$, AR, Aladdin) in deionized water and set volume to 100 ml. Moreover, ammonium succinate (denoted as AS, AR, 99.0%, Aladdin) with different concentration (1 mM, 10 mM, 20 mM) was added into the bare electrolyte to obtain a series of AS-based electrolytes. The most suitable concentration of AS was 10 mM, being marked as $ZnSO_4$ + AS simply and deemed as the main research object. The PANI electrode was obtained by pressing the mixture of PANI, ketjen black and PTFE at a weight ratio of 6:3:1 on the Ti mesh with the active mass loading of about 5 mg cm^{-2}.

Characterizations. Scanning electron microscope (SEM) images were obtained using a field-emission scanning electron microscope (ZEISS Gemini SEM 300, Germany). X-ray diffraction (XRD) patterns were recorded on XRD diffractometer (Bruker D8 Advanced, Germany) with the monochromatic Cu Kα line as the radiation source (λ = 0.15406 nm). Attenuated total reflectance-Fourier transform infrared (ATR-FTIR) spectra of electrolyte were obtained using an FT-IR spectrometer (Nicolet 6700, USA). Raman spectra of different electrolytes were collected on a Reninshaw in Via-Refler instrument with a 532 nm laser. Proton (^{1}H NMR) nuclear magnetic resonance spectra were acquired on a Bruker 600 MHz NMR spectrometer at room temperature. X-ray photoelectron spectra (XPS) were acquired on a XPS spectrometer (ESCALAB 250Xi, Thermo Fisher Scientific, USA) using Mg-Kα radiation as the X-ray source. All XPS spectra were calibrated with the binding energy of 284.8 eV in the C1s spectra. The *in-situ* optical images were recorded on an optical microscope (Yuescope YM710TR), a special microscopy for dendritic observation.

Electrochemical measurements. Zn//Zn symmetric cells, Cu//Zn asymmetric cells and PANI//Zn full cells were assembled in atmospheric environment that using CR2016-type coin cells with a glass fiber membrane as the separator for charge/discharge tests. For Zn//Zn symmetric cells, commercial Zn foils (99.99%, 30 um in thickness) was used as electrode directly. For Cu//Zn asymmetric cells and PANI//Zn full cells, commercial Zn foils (99.99%, 30 um in thickness) were used as anode and commercial Cu foils (9 um in thickness) or PANI electrode were used as cathode. The PANI//Zn cells were tested over the voltage of 0.4-1.49 V. Galvanostatic charge/discharge and long-term performances were tested by battery testing system (LandHe, Wuhan, China; NEWARE, Shenzhen, China). The nucleation overpotential

of Zn was conducted by Cyclic voltammetry (CV) with Cu foil as the working electrode, Zn foil as the counter electrode, and Ag/AgCl as the reference electrode at a scan of 5 mV s^{-1}. Hydrogen evolution reaction and oxygen evolution reaction were recorded at a scanning rate of 5 mV s^{-1} using linear polarization measurement. Tafel plot was recorded with a potential range of −0.2~0.2 V vs. Ag/AgCl at a scan rate of 1 mV s^{-1}. The diffusion behavior of Zn^{2+} was recorded by chronoamperometry (CA) method under the overpotential of −150 mV and a duration of 200 s. Linear polarization curves, CV, CA were tested by a SP-300 electrochemical workstation (Bio-Logic, France).

According to the previous report, the EDLC value was calculated by the following equation:

$$C = i/v$$

where C represents capacitance, v indicates the scan rate (mV s^{-1}), with a range of 8 mV s^{-1}, 10 mV s^{-1}, 12 mV s^{-1}, 14 mV s^{-1}, 16 mV s^{-1}. And i is current density which was defined by half of the difference between positive and negative scanning current at each scanning rate.

Density functional theory (DFT) calculations. We have employed the first-principles tool Vienna Ab initio Simulation Package (VASP) to perform all DFT calculations within the generalized gradient approximation (GGA) using the Perdew-Burke-Ernzerhof (PBE) formulation. We have chosen the projected augmented wave (PAW) potentials to describe the ionic cores and take valence electrons into account using a plane wave basis set with a kinetic energy cutoff of 450 eV. Partial occupancies of the Kohn-Sham orbitals were allowed using the Gaussian smearing method and a width of 0.05 eV. For the optimization of both geometry and lattice size, the Brillouin zone integration was performed with a 0.04 Å^{-1} k-mesh Gamma centered sampling. The self-consistent calculations applied a convergence energy threshold of 10^{-5} eV. The equilibrium geometries and lattice constants were optimized with maximum stress on each atom within 0.02 eV Å^{-1}. The 17 Å vacuum layer was normally added to the surface to eliminate the artificial interactions between periodic images. The weak interaction was described by DFT+D3 method using empirical correction in Grimme's scheme. Spin polarization method was adopted to describe the magnetic system. The adsorption energy of the relevant adsorbent on the Zn (101) was calculated by the equation: E$_{ads}$ = E$_{total}$ − E$_{Zn (101)}$ - E$_{adsorbent}$, where E$_{total}$, E$_{Zn (101)}$ and E$_{adsorbent}$ represent the total energy of molecule or ions adsorbed at Zn (101) surface, the energy of Zn (101) plate, and the energy of the adsorbent molecule, respectively. All calculations were carried out with the Gaussian 16 software. The B3LYP functional with SDD was chosen for Zn, and 6-31G (d, p) basis set for

the other atoms in combination with the GD3BJ dispersion correction. Harmonic vibrational frequency calculations were carried out at the same level of theory for all of the stationary points to verify whether they are local minima and to derive the thermal energy corrections. The singlet point energy calculations were performed with SDD for Zn, and a larger basis set 6-311+g (d, p) for the other atoms. All optimized structures were generated using VESTA.

Molecular dynamics (MD) simulations. The atomistic force field parameters for all ions and molecules are described by the OPLS-AA. The SPC/E water model was adopted in this work. Atomistic simulations were performed using GROMACS package with cubic periodic boundary conditions. The equations for the motion of all atoms were integrated using a classic Verlet leapfrog integration algorithm with a time step of 2.0 fs. A cutoff radius of 1.0 nm was set for short-range van der Waals interactions and real-space electrostatic interactions. The particle-mesh Ewald (PME) summation method with an interpolation order of 4 and a Fourier grid spacing of 0.12 nm was employed to handle long range electrostatic interactions in reciprocal space. In all the three directions, periodic boundary conditions were imposed. Leapfrog algorithm was used to integrate the Newtonian equation of motion. The MD simulation was processed in an NPT ensemble and the simulation time is 20 ns. In NPT simulations, the pressure was maintained at 1 bar by the Berendsen barostat in an isotropic manner and the temperature was maintained by the V-rescale thermostat at 298.15 K. Then, the radial distribution functions (RDF) and the coordination number between Zn^{2+}, SO_4^{2-}, water and AS were calculated.
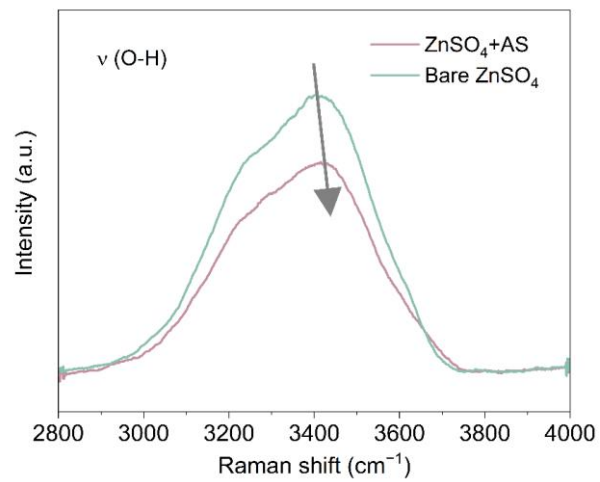
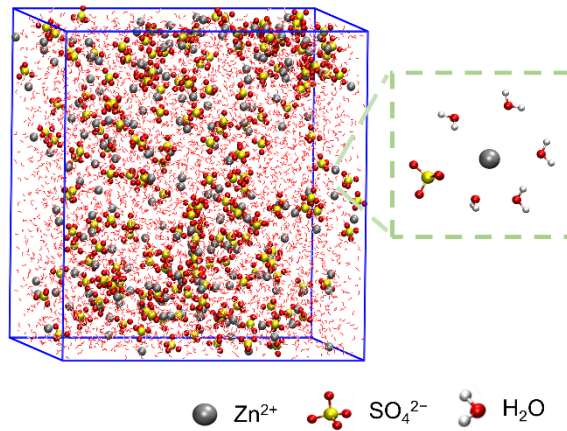**Figure S1.** Raman spectra of ZnSO$_4$ electrolyte with/without 10 mM AS for v(O-H).

Figure S2. 3D snapshot of bare $ZnSO_4$ system obtained from MD simulation and an enlarged snapshot representing Zn^{2+} solvation structure in $ZnSO_4$ electrolyte.
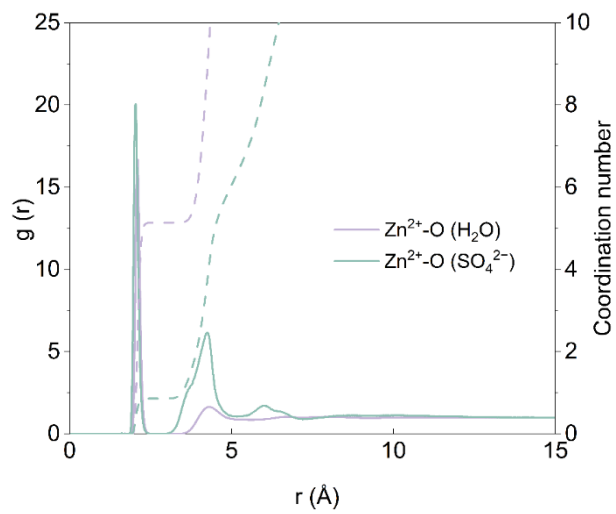
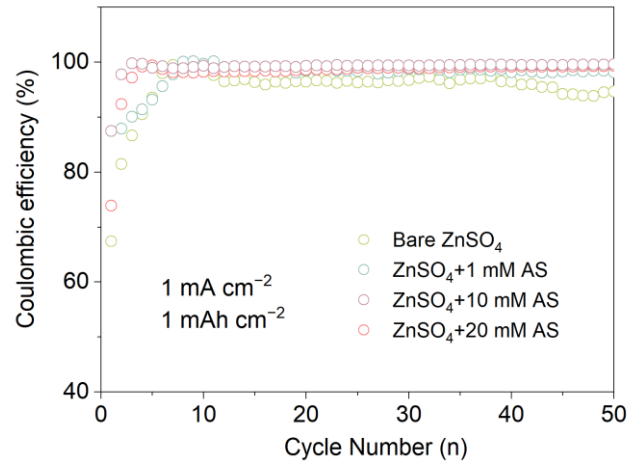**Figure S3.** Radial distribution function (RDF) and coordination number (CN) of Zn^{2+} in bare $ZnSO_4$ electrolyte.

Figure S4. Performance comparison of Cu//Zn asymmetric cells cycled in the ZnSO$_4$ electrolyte with different concentrations of AS additive at 1 mA cm^{-2} and 1 mAh cm^{-2}.
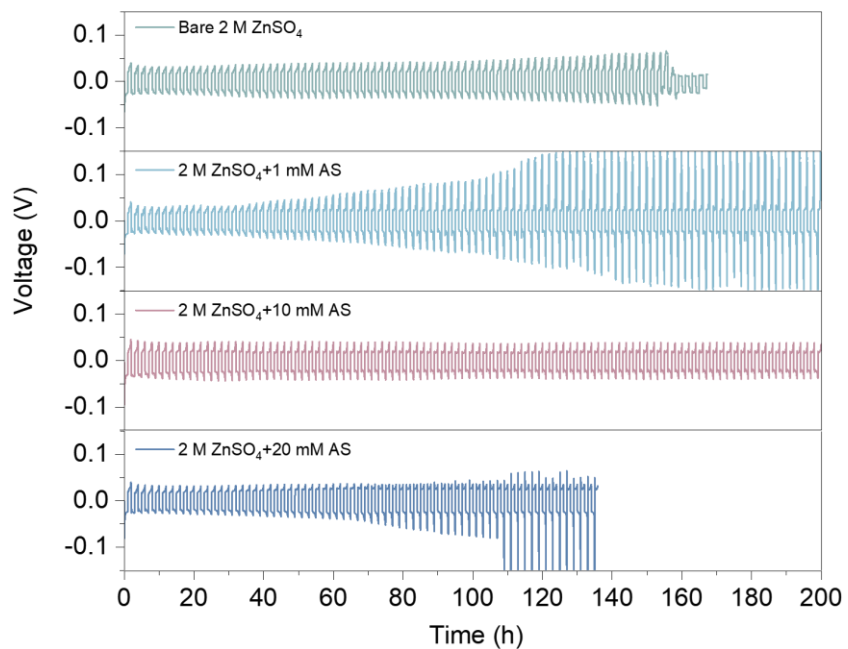
Figure S5. The voltage-time curves of Zn//Zn symmetric cells cycled in 2 M ZnSO₄ containing different contents of AS additives (0 mM, 1 mM, 10 mM and 20 mM) at 1 mA cm^{-2} with 1 mAh cm^{-2}.
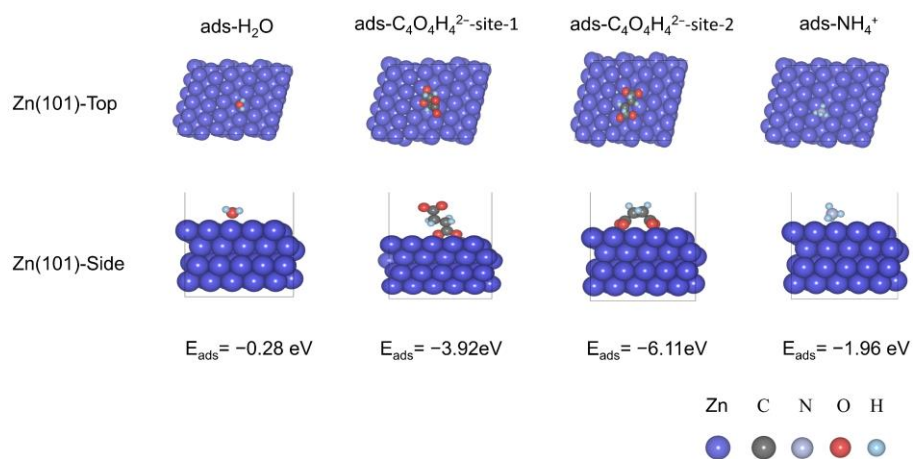
Figure S6. Corresponding adsorption models of various particles on Zn (101) plane at two different viewing angles, and succinate anion ($C_4O_4H_4^{2-}$) includes two adsorption situations.
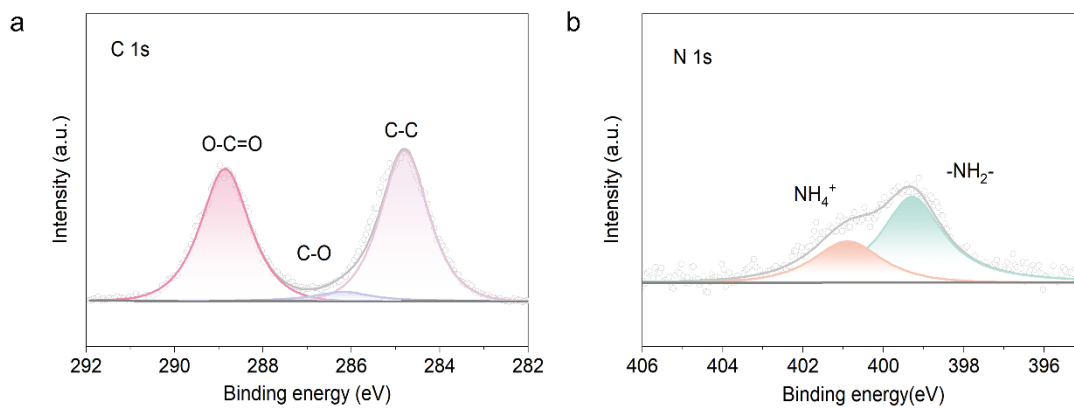
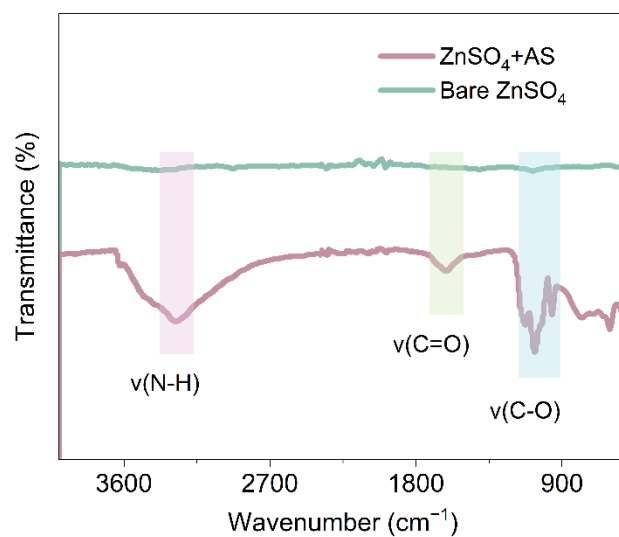**Figure S7.** XPS spectra of (a) C 1s, (b) N 1s of ammonium succinate powder.

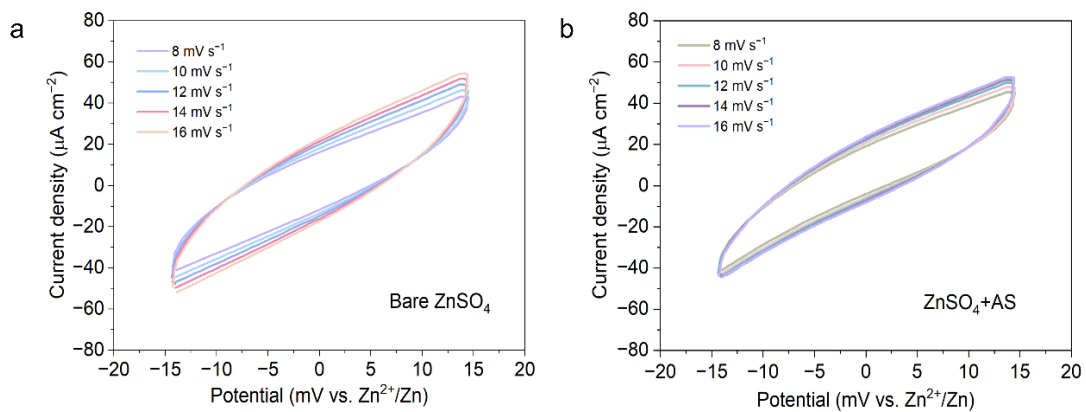**Figure S8.** FT-IR spectra of Zn electrode surface after soaked in $ZnSO_4$ electrolyte with/without AS additive.

Figure S9. CV curves for Zn//Zn symmetric cells in the range of −15 mV and 15 mV under various scan rates in (a) Bare ZnSO$_4$, (b) ZnSO$_4$+AS.
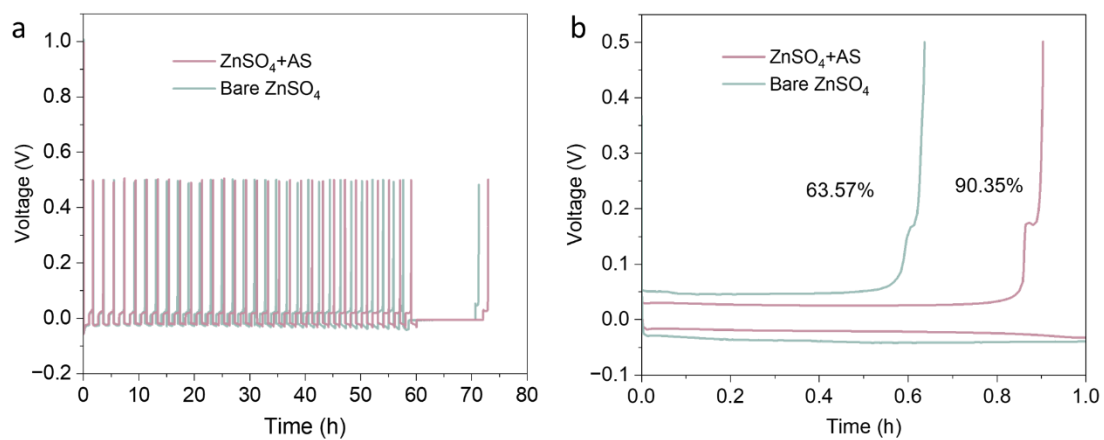
Figure S10. Self-discharge behavior of Cu//Zn cells in 2 M $ZnSO_4$ with/without 10 mM AS additive.
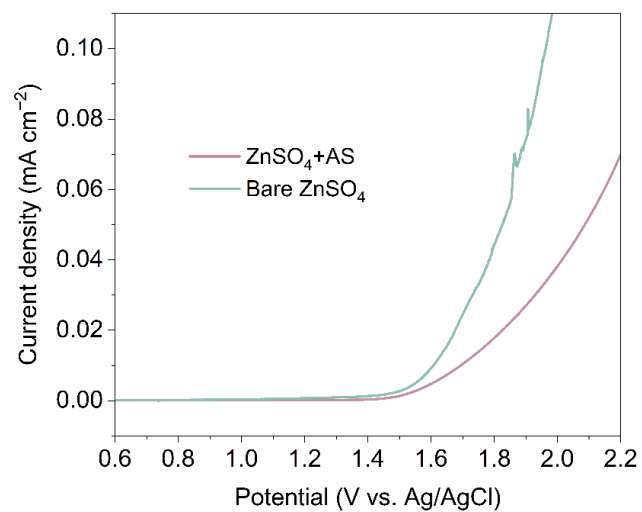
Figure S11. Oxygen evolution reaction (OER) curves of $ZnSO_4$ electrolyte with/without AS additive.

initial state   discharging for 5 s   discharging for 10 s   discharging for 1 min   discharging for 2 min   after shaking
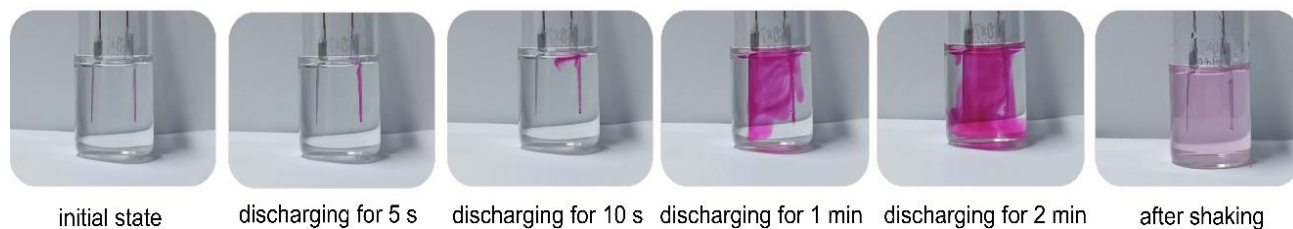
Figure S12. Visualization of pH fluctuation at zinc electrode surface in $ZnSO_4$+SS electrolyte. (left electrode: Zn counter electrode; right electrode: Zn working electrode)
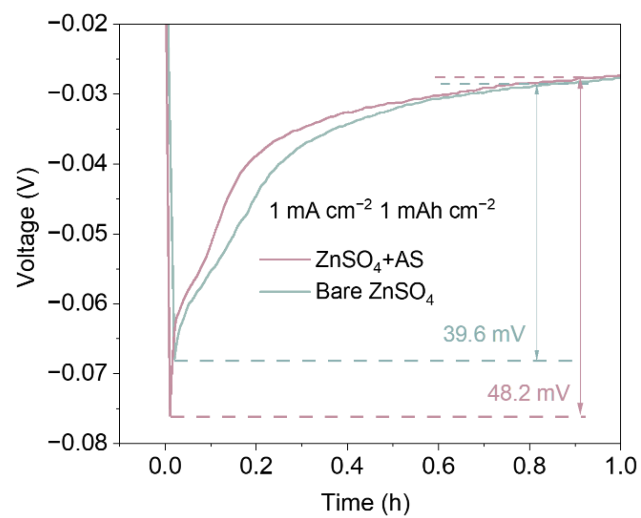
Figure S13. The plating voltage profiles of Zn//Zn symmetric cells at 1 mA cm^{-2} and 1 mAh cm^{-2} for initial nucleation process with different electrolytes.
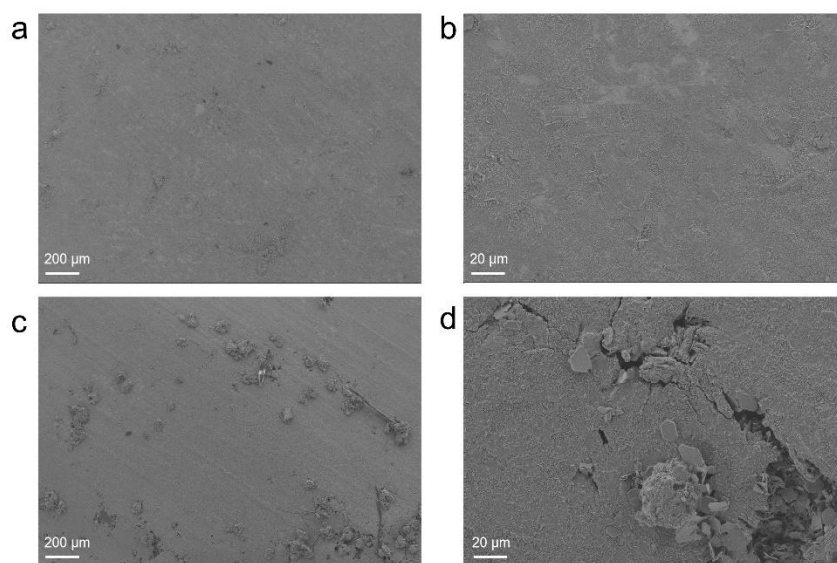
Figure S14. SEM image of Zn anode after 20 cycles in (a, b) $ZnSO_4$+AS and (c, d) Bare $ZnSO_4$ at current density of 1 mA cm^{-2} and plating capacity of 1 mAh cm^{-2}.
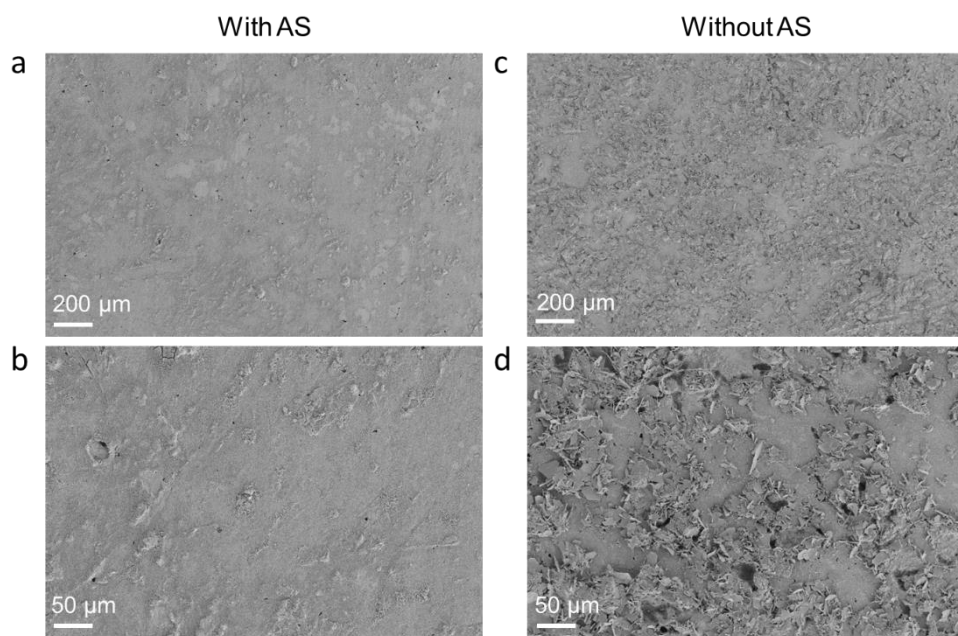
Figure S15. SEM images of Zn electrode after cycling in 2 M ZnSO$_4$ with AS (a, b) or without AS (c, d) under a high current density of 10 mA cm^{-2} with deposition capacity of 2 mAh cm^{-2}.
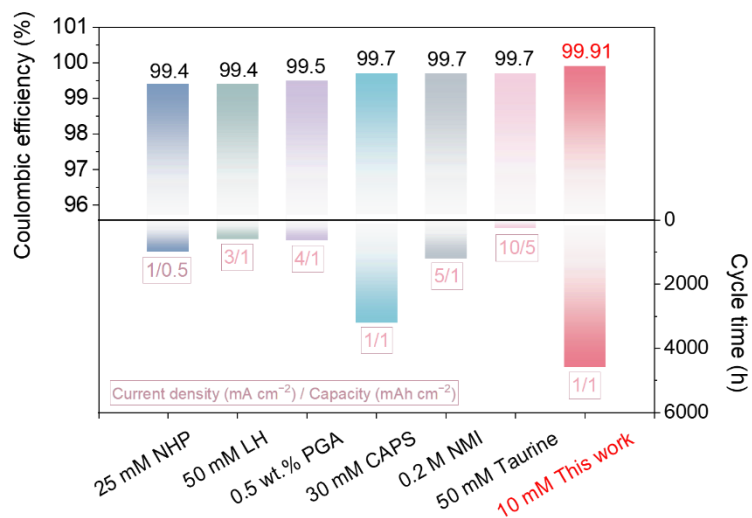
Figure S16. Comparison of CE and cycle time in Cu//Zn cells with other additives having pH buffering ability.[1-6] Comparing with other additives having pH buffering ability, ammonium succinate with lowest usage amount shows highest coulombic efficiency. Noted that the high coulombic efficiency was obtained at low current density of 1 mA cm⁻², while the coulombic efficiency for others additives were obtained at higher current density. Above results indicate the unique advantage of AS additive.
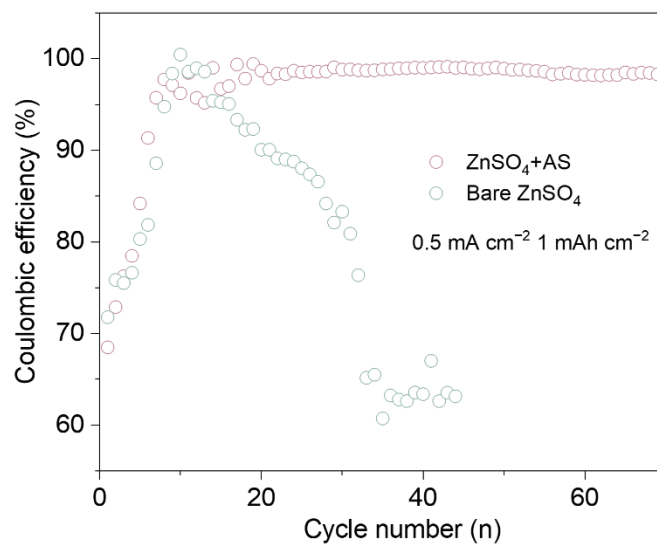
Figure S17. Long-time cycle performance of 2 M $ZnSO_4$ with/without AS additive at low current density of 0.5 mA cm^{-2} with deposition capacity of 1 mAh cm^{-2}.
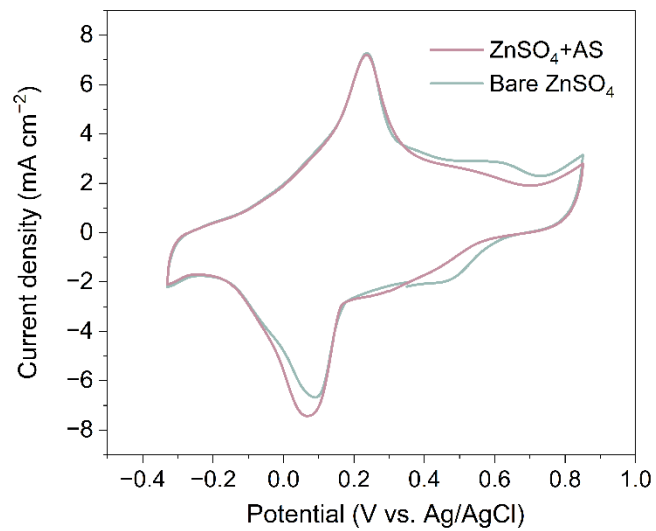
Figure S18. CV curves of PANI cathode in different electrolyte (PANI: working electrode, AC: counter electrode, and Ag/AgCl as reference electrode).

Note 1. Discussion on judgement standard for trace amount additive

We have reviewed relevant papers, and found that there is no explicit standard to judge what amount of additive can be called as "trace amount". Generally, these references can be categorized into three kinds according to different concentration units: (1) mmol L^{-1} (mM). The concentration of additive in Ref. 7 is 10 mM, it was called as trace additive; (2) g L^{-1}. The amount of additive is 1.8 g L^{-1} and 10 g L^{-1} in Ref. 8 were called as trace amount; (3) wt.%. The amount of additive is 2 wt.% in Ref. 9, still it was called as trace additive. Based on above analysis, ammonium succinate (10 mM/1.5 g L^{-1}/0.1 wt.%) we used in this paper also can be considered as trace additive.

References

1 W. Zhang, Y. Dai, R. Chen, Z. Xu, J. Li, W. Zong, H. Li, Z. Li, Z. Zhang, J. Zhu, F. Guo, X. Gao, Z. Du, J. Chen, T. Wang, G. He and I. P. Parkin, *Angew. Chem., Int. Ed.*, 2023, **62**, e202212695.

2 Y. Wang, T. Wang, Y. Mao, Z. Li, H. Yu, M. Su, K. Ye, D. Cao and K. Zhu, *Adv. Energy Mater.*, 2024, **14**, 2400353.

3 C. Huang, J. Mao, S. Li, W. Zhang, X. Wang, Z. Shen, S. Zhang, J. Guo, Y. Xu, Y. Lu and J. Lu, *Adv. Funct. Mater.*, 2024, **34**, (26). DOI: 10.1002/adfm.202315855.

4 C. Liu, D. Xie, W. B. Jiang, W. Y. Diao, F. Y. Tao, X. Z. Wang, H. Z. Sun, W. L. Li, X. L. Wu and J. P. Zhang, *Energy Storage Materials*, 2024, **70**, DOI: 10.1016/j.ensm.2024.103497.

5 M. Zhang, H. Hua, P. Dai, Z. He, L. Han, P. Tang, J. Yang, P. Lin, Y. Zhang, D. Zhan, J. Chen, Y. Qiao, C. C. Li, J. Zhao and Y. Yang, *Adv. Mater.*, 2023, **35**, e2208630.

6 K. Ouyang, S. Chen, W. Ling, M. Cui, Q. Ma, K. Zhang, P. Zhang and Y. Huang, *Angew. Chem., Int. Ed.,* 2023, **62**, e202311988.

7 M. C. Han, J. H. Zhang, C. Y. Yu, J. C. Yu, Y. X. Wang, Z. G. Jiang, M. Yao, G. Xie, Z. Z. Yu and J. Qu, *Angew. Chem., Int. Ed.*, 2024, **63**, e202403695.

8 H. B. Chen, H. Meng, T. R. Zhang, Q. Ran, J. Liu, H. Shi, G. F. Han, T. H. Wang, Z. Wen, X. Y. Lang and Q. Jiang, *Angew. Chem., Int. Ed.*, 2024, **63**, e202402327.

9 X. Zhao, Y. Wang, C. Huang, Y. Gao, M. Huang, Y. Ding, X. Wang, Z. Si, D. Zhou and F. Kang, *Angew. Chem., Int. Ed.*, 2023, **62**, e202312193.